Supplement of Hydrol. Earth Syst. Sci., 28, 5133–5147, 2024
https://doi.org/10.5194/hess-28-5133-2024-supplement

Hydrology and Earth System Sciences
Open Access
EGU

Supplement of

On the cause of large daily river flow fluctuations in the Mekong River

Khosro Morovati et al.

Correspondence to: Fuqiang Tian (tianfq@mail.tsinghua.edu.cn)

The Supplementary Material contains the following items:

S1. Additional information for developed hydrodynamic model
S2. A figure for the storage of tributary dams
S3. Bathymetry data
S4. Additional figures for the developed hydrodynamic model
S5. Additional figures for the THREW hydrological model
S6. Additional figures for large water level/flow changes
S7. Additional figures for the contribution of sub-basins to mainstream flow
S8. Additional figures for each event resulting in daily water level increases for all stations
S9. A figure for the precipitation trend
S10. Additional details for Figures 6 and 11

S1. Additional information for developed hydrodynamic model

S1.1 Numerical set-up

The impermeable riverbed was addressed by setting the vertical velocity relative to the reference planes to zero. Following this, the subsequent boundary conditions were defined for the momentum equations in the following manner:

$$(\frac{\upsilon_V}{H}\frac{\partial u}{\partial \sigma})_{\sigma=-1} = \frac{1}{\rho_0}\tau_{b\zeta} \qquad and \qquad (\frac{\upsilon_V}{H}\frac{\partial v}{\partial \sigma})_{\sigma=-1} = \frac{1}{\rho_0}\tau_{b\xi} \tag{1}$$

where $\tau_{b\zeta}$ and $\tau_{b\xi}$ represent the components of the bed stress.

The two-equation model, referred to as the $k-\varepsilon$ turbulence model, enables the separate calculation of k and ε using Equations 2 and 3, respectively. Within this model, the production and dissipation terms are the primary factors. Additionally, the vertical length scales are noted to be smaller than their horizontal counterparts.

$$\frac{\partial k}{\partial t} + \frac{u}{R\cos\phi}\frac{\partial k}{\partial \lambda} + \frac{\upsilon}{R}\frac{\partial k}{\partial \eta} + \frac{w}{d+\partial \sigma}\frac{\partial k}{\partial \sigma} = \frac{1}{(d+\zeta)^2}\frac{\partial}{\partial \sigma}(D_k\frac{\partial k}{\partial \sigma}) + P + P + B - \varepsilon \tag{2}$$

$$\frac{\partial \varepsilon}{\partial t} + \frac{u}{R\cos\phi}\frac{\partial \varepsilon}{\partial \lambda} + \frac{\upsilon}{R}\frac{\partial \varepsilon}{\partial \eta} + \frac{w}{d+\zeta}\frac{\partial \varepsilon}{\partial \sigma} = \frac{1}{(d+\zeta)^2}\frac{\partial}{\partial \sigma}(D_\varepsilon\frac{\partial \varepsilon}{\partial \sigma}) + P_\varepsilon + P_{\varepsilon w} - B_\varepsilon - c_{2\varepsilon}\frac{\varepsilon^2}{k} \tag{3}$$

S1.2 Meshing

Splines were delineated along the land boundaries, aligned with the flow path. The meshing of the computational domain was executed to meet the smoothness and orthogonality requirements of the spherical system. A 3D mesh was generated in spherical coordinates for the computational domain, comprising 10 layers for river depth, which remained constant for the river length representing each sub-basin. For the river width, the same number of cells (50 cells) was employed from JingHong to Kratie stations, as the computational domain in the river width direction remained unchanged at 2 km. In contrast, for the river length, since each sub-basin was simulated independently, the number of cells varied according to the river length of each sub-basin; nevertheless, the cell length remained constant at 40 m.

S2. A figure for the storage of tributary dams

Attributes for all tributary dams are not available. Figure S1 shows the total storage capacity for 83 tributary dams. Xe Kaman and Nam Ngum tributary dams located in Laos have the highest storage capacity than other dams, with 4.8 km^3 and 4.7 km^3, respectively.

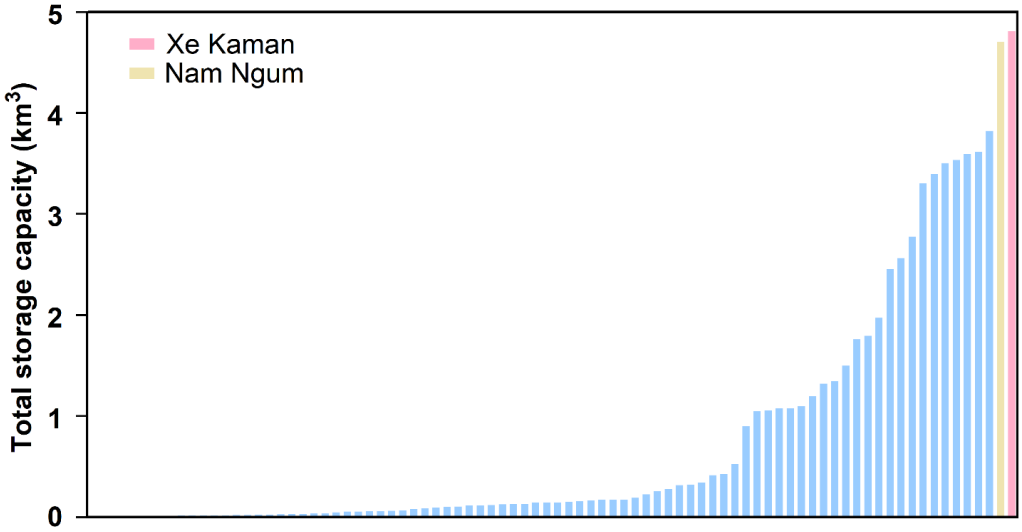

Figure S1. Illustrates of the total storage capacity of tributary dams along the Mekong River. Please note that attributes for all tributary dams are not available, and this figure represents data solely for the available dams.

S3. Bathymetry

While the lower Mekong generally exhibits placid conditions, the depth representation may vary across the river, potentially impacting flow dynamics. As such, reliable bathymetry data are essential. For the surrounding areas, data from the Shuttle Radar Topography Mission (SRTM) with an original resolution of 90 meters were employed. However, the density of this bathymetry data was insufficient compared to the resolution of the defined mesh. To address this, interpolation using the triangular technique was employed, supplemented by the internal diffusion method to assign depths to non-interpolated areas (refer to Deltares, 2014 for detailed information).

For the river, cross-sectional shapes were available at various stations, and an anisotropy approach was adopted during depth interpolation due to its superior performance in the flow-oriented coordinate system (see Merwade et al., 2006). To replicate digital elevation models (DEMs) in areas lacking bathymetry data, the RGFGRID tool integrated into Delft3D-Flow was utilized to establish an orthogonal grid system (refer to Deltares, 2014).

Figure S2 illustrates a comparison between the predicted cross-section at the Pakse (PA) station and the measured cross-section. It is evident that, although there are some discrepancies, the overall shape of the predicted cross-section closely resembles that of the measured one.

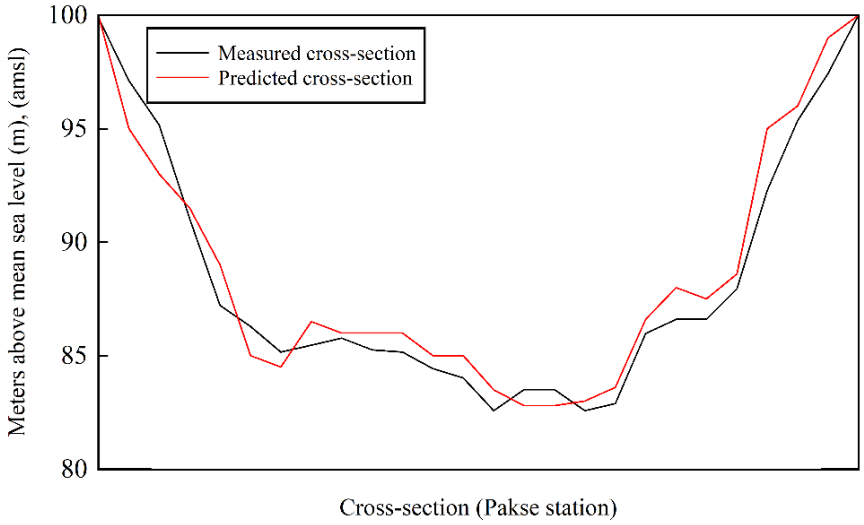

Figure S2. A comparison between the measured bed profile and the predicted profile at the Pakse (PA) station.

S4. Additional figures for the developed hydrodynamic model

One important factor influencing the accuracy of the hydrodynamic models is mesh size, which needs to be defined for the computational domain. Various mesh sizes were analyzed and tested to produce results that closely match the measured data. A mesh convergence assessment was conducted, evaluating different sizes for the depth, length, and width of the river. The entire river stretch from JingHong to Kratie was divided into blocks, with each block containing a specific number of cells for river width and flow direction. Table S3 presents three selected mesh configurations to achieve an optimal computational domain for the model.

Table S1. Information on the cell sizes used for mesh convergence assessment. '*L*' represents the number of vertical layers. Note that the same number of cells was defined for each block in the flow direction.

Mesh number	No. of cells for the width of each block	Cell size (m)	*L*
1	30	66.6	8
2	50	40	10
3	70	28.6	12

Figure S3 presents the results of water level and velocity comparisons among the three selected mesh configurations listed in Table S1. The observations indicate that mesh refinement enhances the accuracy of water level and velocity simulations. Specifically, for water level, the Mean Relative Error (MRE) decreases from 13.5% with Mesh 1 to 6.2% with Mesh 2. Similarly, for velocity, a point-by-point comparison shows a reduction in MRE from 17.2% with Mesh 1 to 5% with Mesh 2. However, further refinement from Mesh 2 to Mesh 3 does not yield significant improvement. Consequently, Mesh 2 is chosen for all simulations in this study. To better illustrate how cell size influences water levels, the authors have chosen to present the water level profile results for one month.

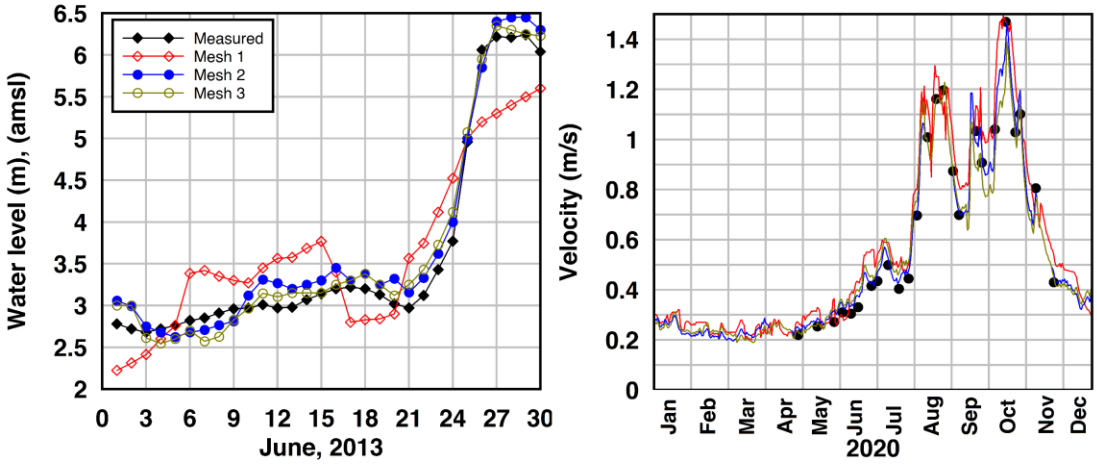

Figure S3. Mesh sensitivity analysis for water level (Mukdahan (MD) station) and velocity (Stung Treng (ST) station).

Figure S4 illustrates the comparison between the velocity profiles obtained from the hydrodynamic model and the measured values for the years 2018 and 2019 at the Stung Treng (ST) station. A detailed point-by-point comparison indicates a relatively high level of accuracy, with mean relative errors of 5.5% and 7.1% for the data from 2019 and 2018, respectively.

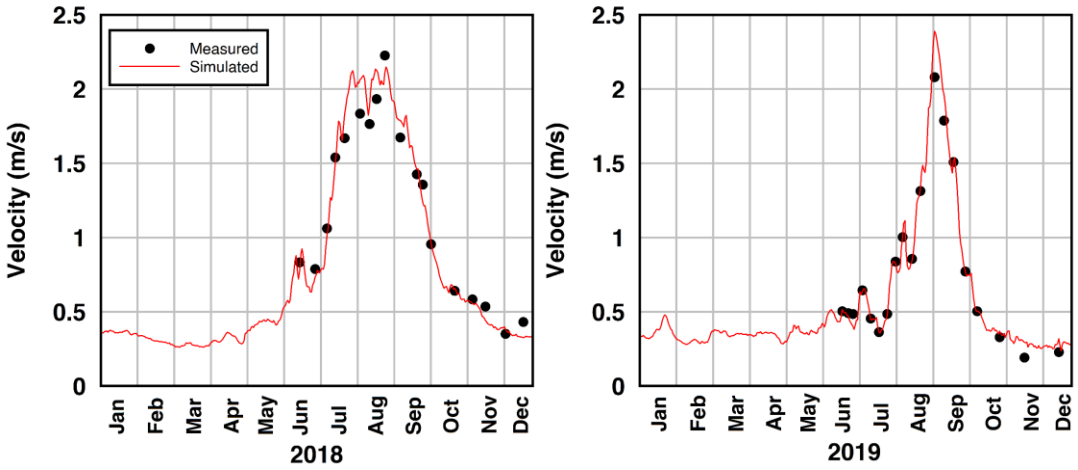

Figure S4: A point-by-point comparison of measured velocity data with hydrodynamic model for the years 2019 (part a) and 2020 (part b) at Stung Treng station.

The comparison between water levels yielded by the hydrodynamic model and the measured ones demonstrates a high level of accuracy, with an NSE exceeding 0.94. The model accurately captures both high and low flows throughout the wet and dry seasons.

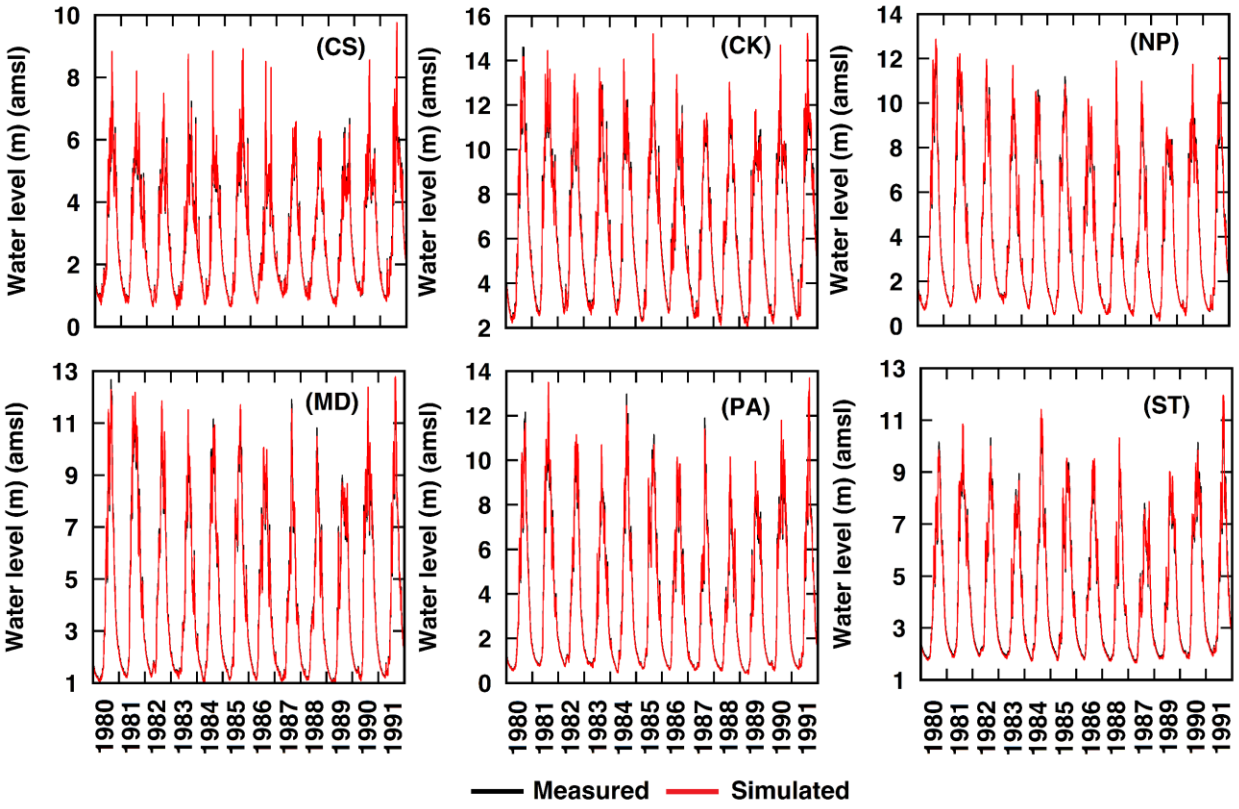

Figure S5: A comparison of measured water levels with those obtained by the hydrodynamic model for mainstream stations. CS, CK, NP, MD, PA, and ST represent Chiang Saen, Chiang Khan, Nakhon Phanom, Mukdahan, Pakse, and Stung Treng stations, respectively.

S5. Additional figures for the THREW hydrological model

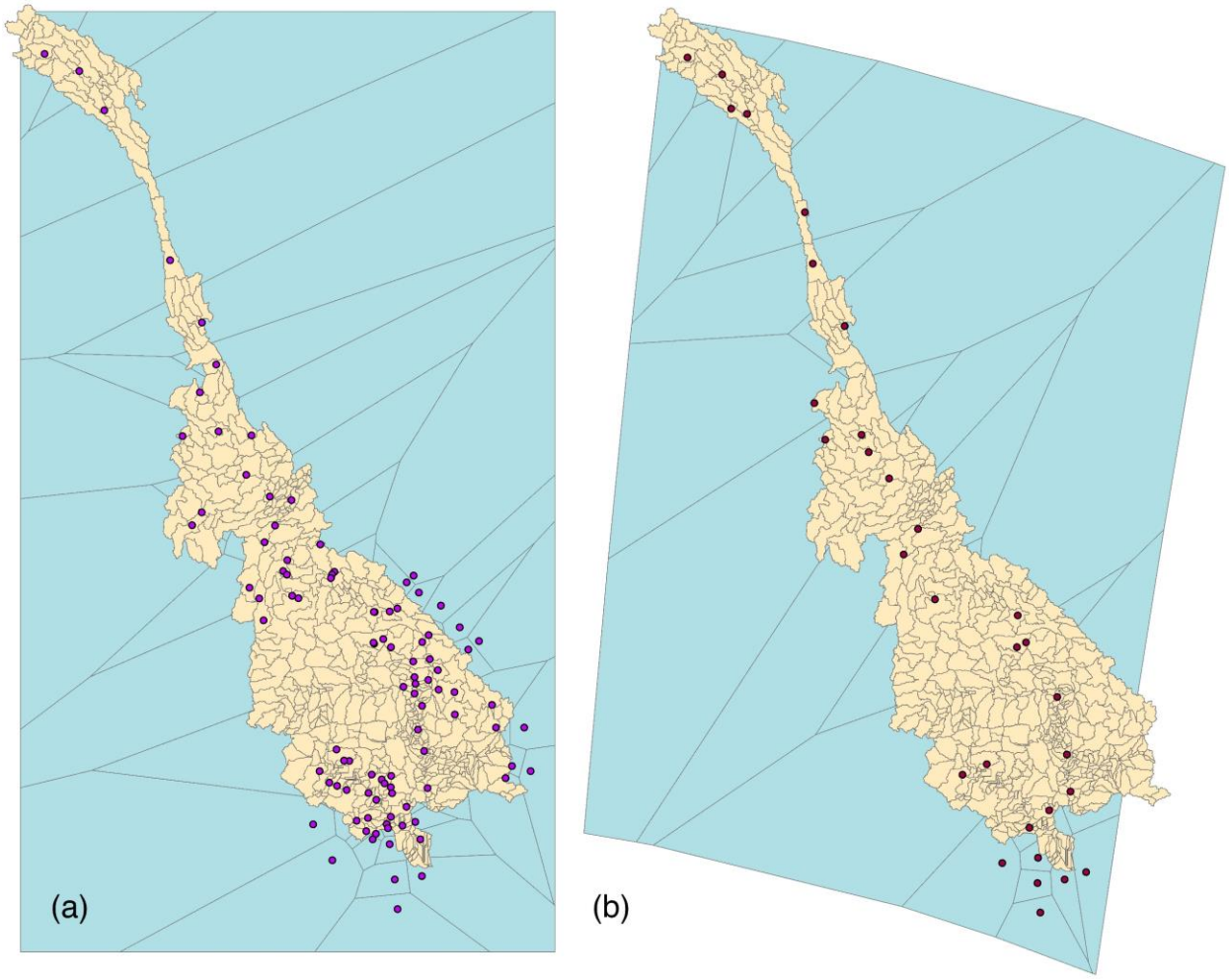

Figure S6: The location of stations for meteorological data including (a) precipitation and (b) meteorological data including near-surface air pressure, air temperature, specific humidity, wind speed and direction, sunshine duration, and solar radiation.

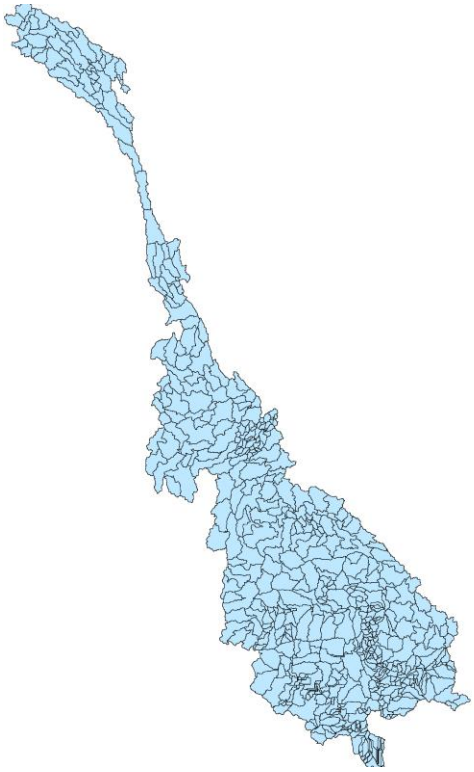

Figure S7: 651 REWs covering the LMR in the THREW hydrological model

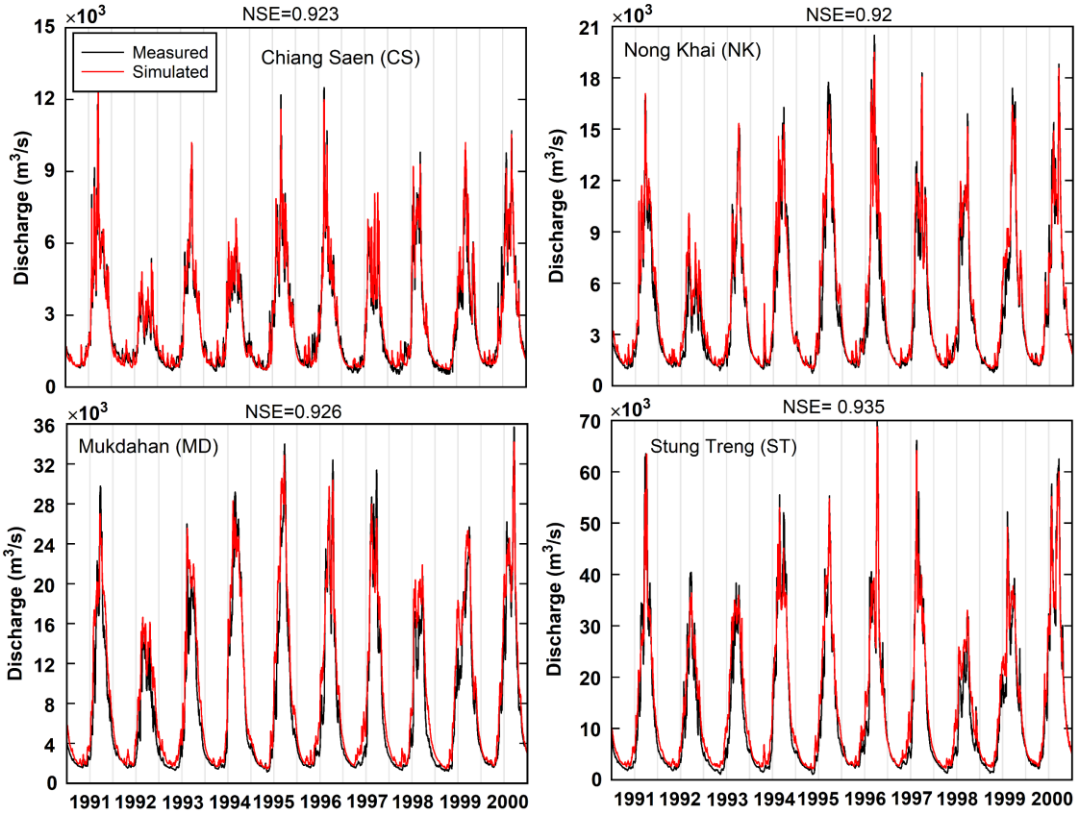

Figure S8. Comparison of the produced discharge data using the THREW hydrological model at mainstream stations of the LMR with measured data.

Figure S9 shows the discharge data produced for six tributary stations along the LMR, utilizing the THREW hydrological model. It is evident from the figures that the model has captured both high and low-flow events across various years. The NSE values, indicating model performance, are consistently high, surpassing 0.88.

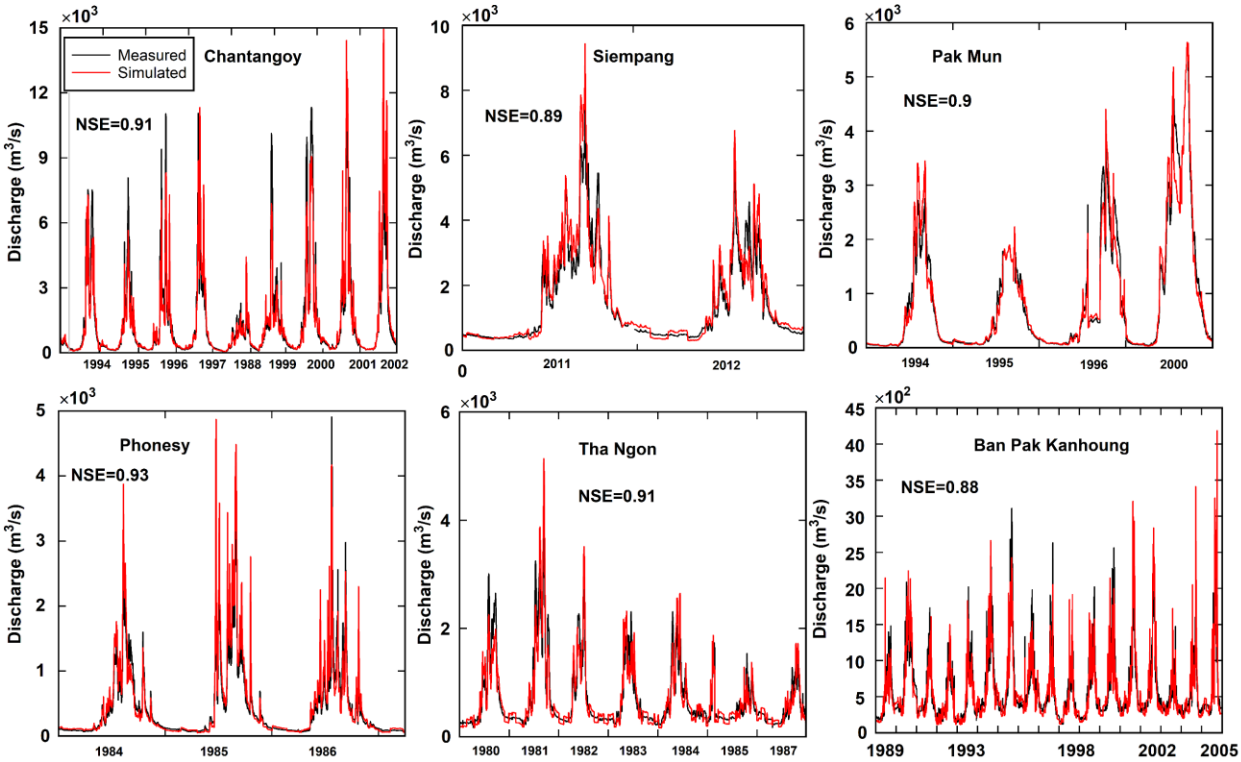

Figure S9. Comparison of the produced discharge data using the THREW hydrological model at tributaries across the Mekong River with measured data.

S6. Additional figures for large water level/flow changes

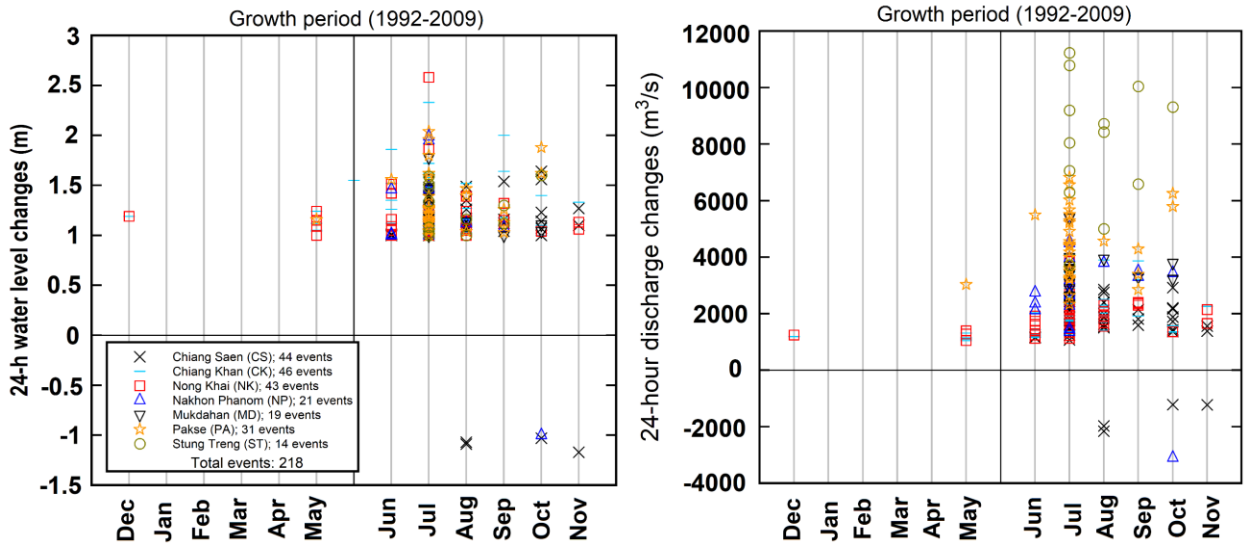

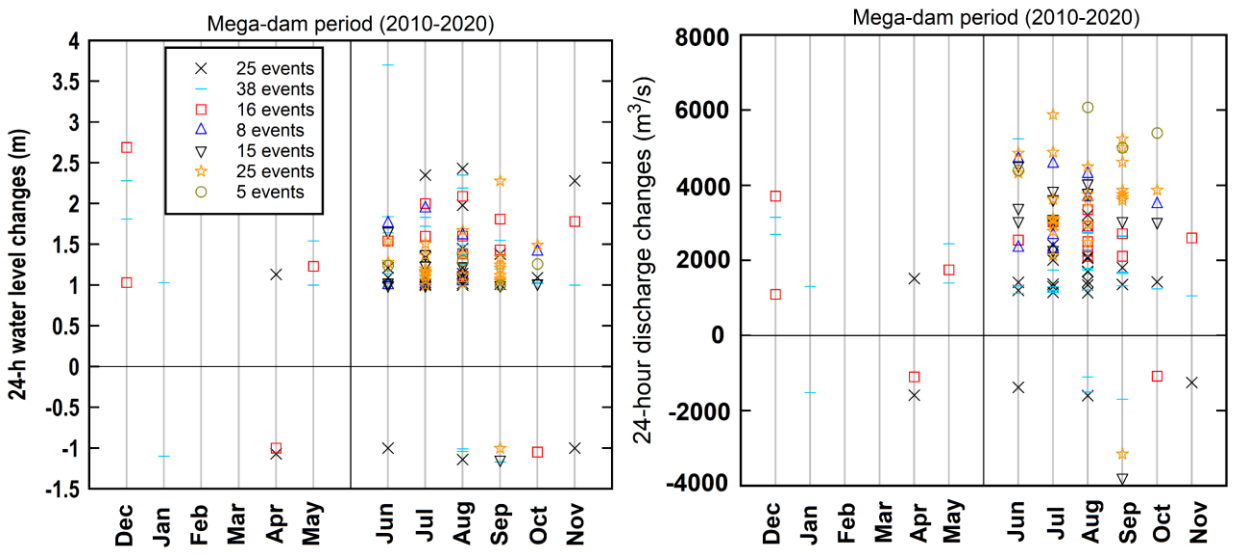

Figure S10. Large daily water level/flow changes during the mega-dam and growth periods for all mainstream stations.

S7. Additional figures for the contribution of sub-basins to mainstream flow

Figure S11 illustrates the contribution of each sub-basin and upstream station to the total discharge passing through each station. While a nearly identical contribution is observed compared to the pre-dam period, there has been a reduction in the total discharge passing through mainstream stations during the mega-dam period compared to the two previous periods. For instance, at Stung Treng (ST) station, the mean discharge during the wet season decreased by approximately 5.1%, and during the dry season by about 10.7% in the mega-dam period compared to the pre-dam period, resulting in a reduction from 24,130 m^3/s to 22,896 m^3/s during the wet season and from 4,849 m^3/s to 4,326 m^3/s during the dry season.

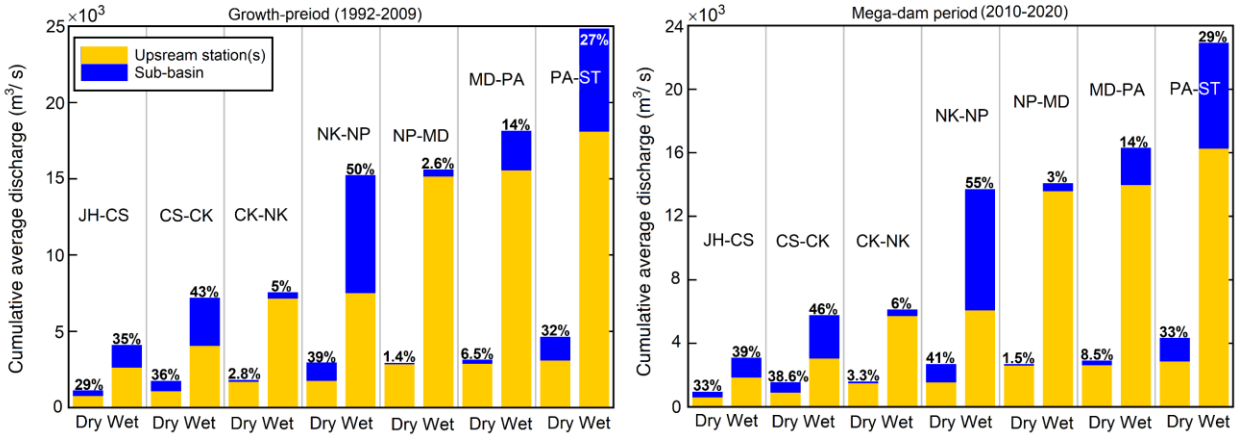

Figure S11. The cumulative average discharge data at each hydrological station along the river's mainstream during wet and dry seasons for the growth and mega-dam periods, incorporating contributions from both the corresponding sub-basin and its upstream station.

S8. Additional figures for each event resulting in daily water level increases for all stations

Figures S12a to g depict the analysis conducted for each event during the defined periods at each mainstream station. It is observed that Stung Treng (ST) has encountered the lowest number of daily river flow increases resulting in water level changes exceeding 1 meter. With the exception of Mukdahan (MD) and NongKhai (NK) stations, which are

located close to their upstream station and have relatively small sub-basins compared to other stations, the contribution of other sub-basins to downstream large daily river flow increases is more significant.

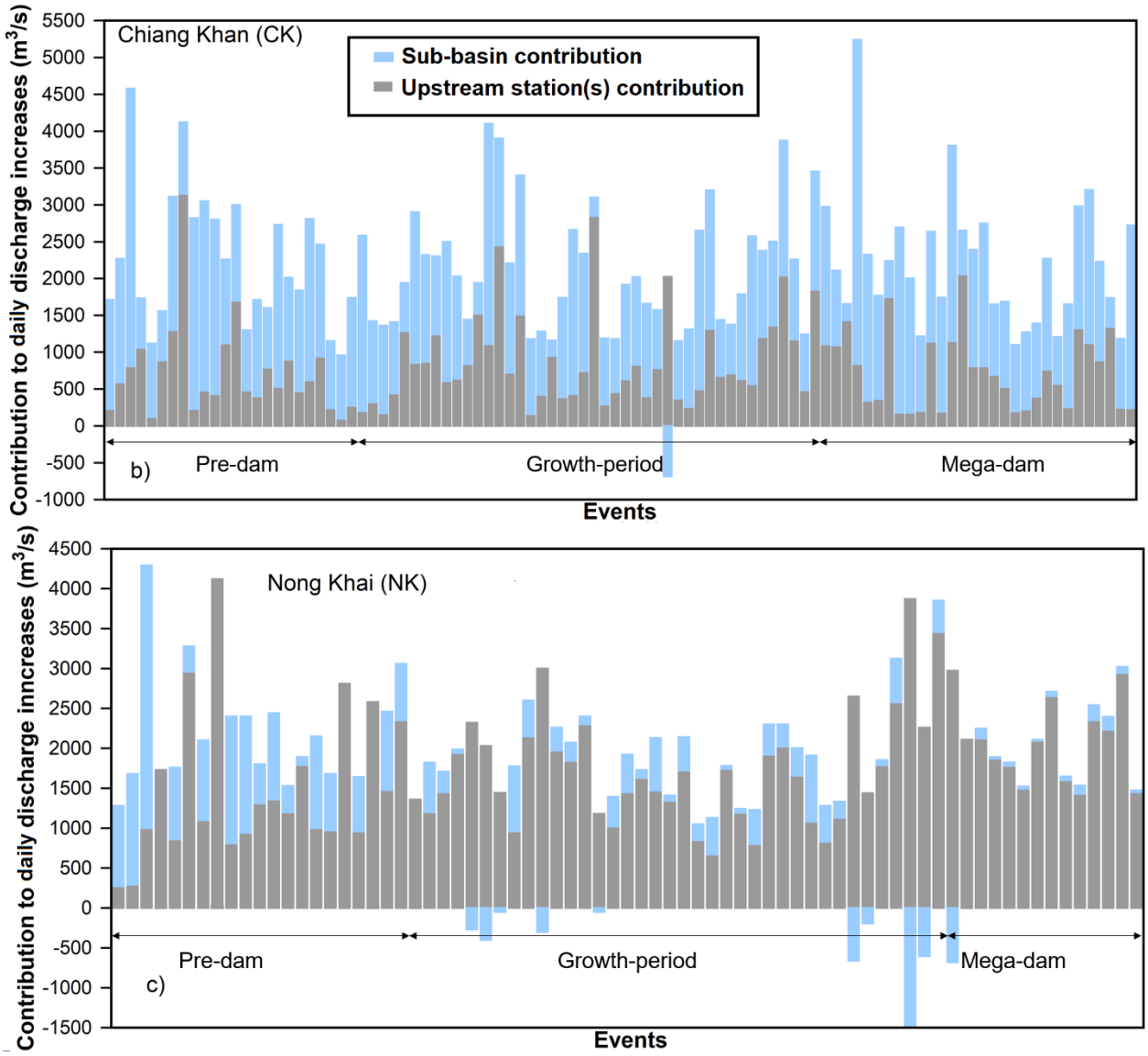

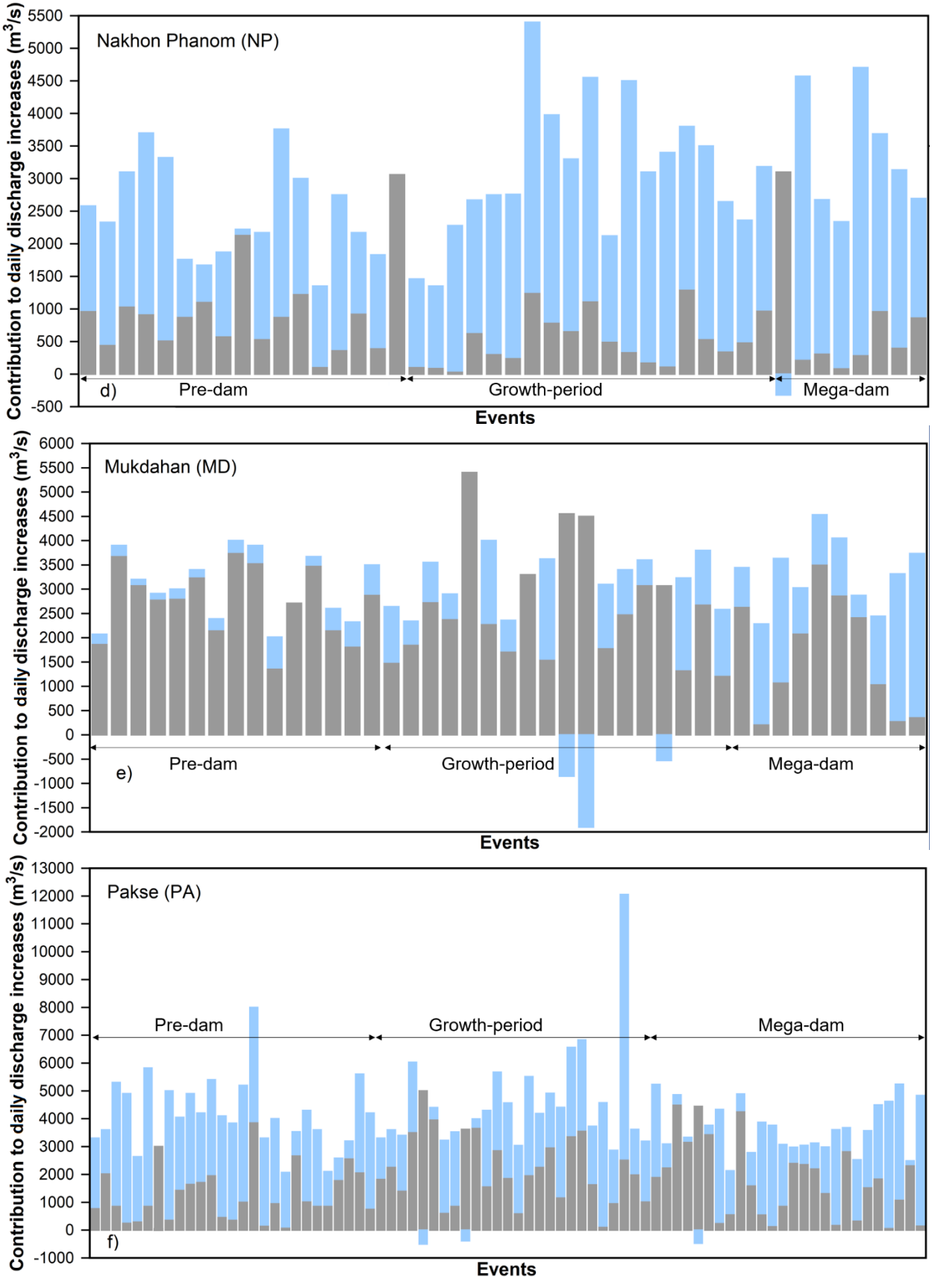
Nakhon Phanom (NP)
Contribution to daily discharge increases (m3/s)
5500
5000
4500
4000
3500
3000
2500
2000
1500
1000
500
0
-500
d)
Pre-dam
Growth-period
Mega-dam
Events
Mukdahan (MD)
Contribution to daily discharge increases (m3/s)
6000
5500
5000
4500
4000
3500
3000
2500
2000
1500
1000
500
0
-500
-1000
-1500
-2000
e)
Pre-dam
Growth-period
Mega-dam
Events
Pakse (PA)
Contribution to daily discharge increases (m3/s)
13000
12000
11000
10000
9000
8000
7000
6000
5000
4000
3000
2000
1000
0
-1000
Pre-dam
Growth-period
Mega-dam
f)
Events

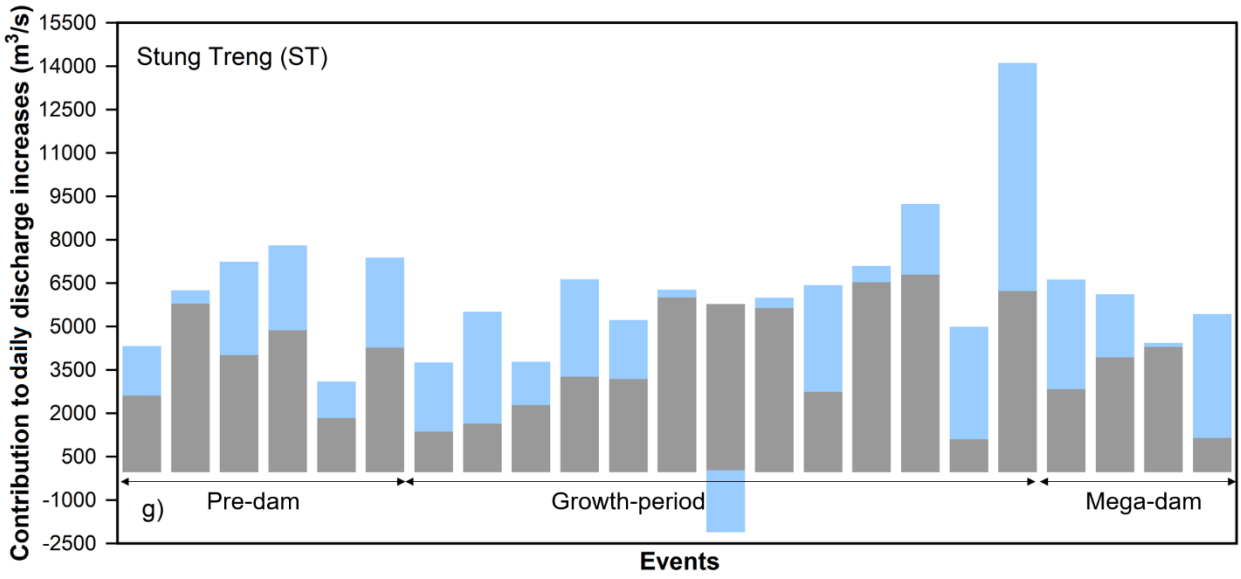

Figure S12. Event analysis for large daily river flow increases, leading to water level rises exceeding 1 meter, across the pre-dam period, growth period, and mega-dam period.

S9. A figure for the precipitation trend

Figure S13 illustrates the estimated precipitation received in the JH-CS sub-basin during July 1986. Despite fluctuations, precipitation in this month exhibited a consistent upward trend until two notable river flow shifts, each exceeding a water level increase of >1m at the CS station. Analysis indicated that such patterns were frequent in the basin, potentially contributing to a higher occurrence of increased events compared to reduction events.

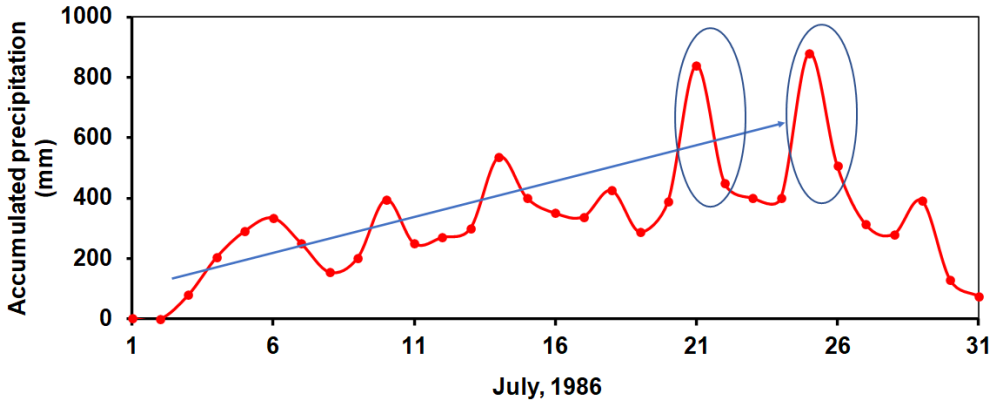

Figure S13. The trend of precipitation received in the JH-CS subbasin in July 1986 resulted in water level increases of greater than 1 m.

S10. Additional details for Figures 6 and 11

In Figure 6, we utilized the observed upstream discharges as inlet boundaries for the hydrodynamic model and calculated the response time for various events. Subsequently, we used the observed discharge and the derived response time to generate correlations in Excel. We determined that the "power correlation" best represents the relationship between upstream discharge and the time required for propagation to the downstream station. R^2 values were calculated for all events at each station using Excel. The same approach was followed in Figure 11.